Extreme resilience and dissipation in heterogeneous elasto-plastomeric crystals

Supplementary Information

Gisoo Lee,[a] Jaehee Lee,[a] Seunghyeon Lee,[a] Stephan Rudykh,[b] and Hansohl Cho[*a]

[a] Department of Aerospace Engineering, Korea Advanced Institute of Science and Technology, Daejeon, 34141, Republic of Korea

[b] Department of Mechanical Engineering, University of Wisconsin, Madison, WI 53706, USA

[*]E-mail: hansohl@kaist.ac.kr

1 Large strain mechanical behavior of hard and soft materials: experiments and constitutive models

Here, we present the large strain mechanical behavior of the hard and soft materials; hard: mixture of TangoPlus and VeroWhitePlus, soft: TangoPlus. Cylindrical samples of the hard and soft materials were printed with an aspect ratio of 1.0 in order to avoid local buckling and distortion and to achieve homogeneous deformation. Then, the samples were compressed in a testing machine and the load-displacement data were collected under cyclic deformation conditions. Fig. S1 presents the stress-strain curves of hard and soft materials under uniaxial compression at an engineering strain rate of 0.05 s^{-1}. The hard material exhibits a relatively stiff initial elastic response followed by an yield-like stress-rollover and post-yield hardening at increasing strains. Upon unloading, the hard material exhibits "plastomeric" features including large energy dissipation accompanied by significant residual strain. The hard material was found to recover their original shapes in a few hours after the end of unloading. By contrast, the soft material exhibits much more compliant response. Upon unloading, there is energy dissipation negligible compared to that in the hard material. Furthermore, the soft material recovers their original shape immediately upon unloading; the soft material exhibits purely "elatomeric" features, also known as hyperelasticity upon large strain loading and unloading conditions.
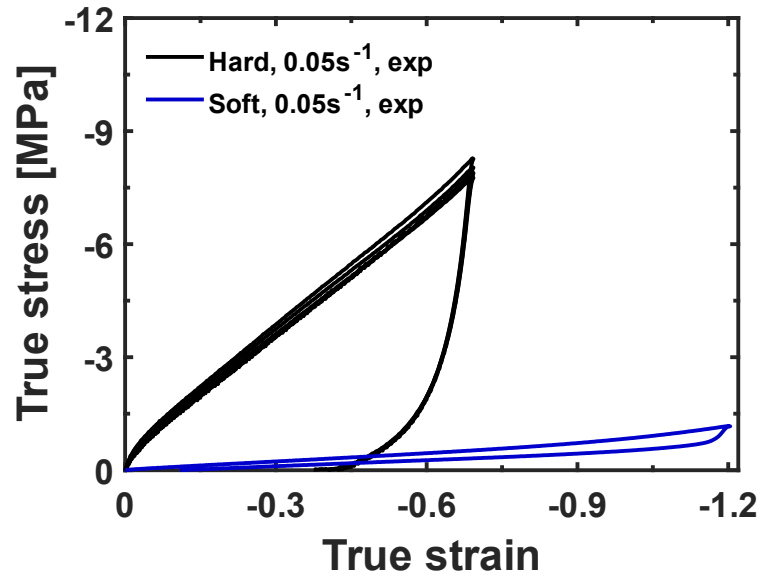
1

Fig. S1: Stress-strain behavior of the hard material (black solid line) and the soft material (blue solid line) at a strain rate of 0.05 s^{-1} in experiment.

We then present finite deformation constitutive modeling framework for the hard and soft materials. For the hard material, we employed multiple micro-rheological mechanisms to describe the elastic and inelastic resistances as schematically illustrated in Fig. S2. It comprises (1) a time-dependent elasto-viscoplastic mechanism (denoted I) and a time-independent hyperelastic mechanism (denoted N). We then define the following basic fields:

$$\mathbf{F} = \nabla\varphi(\mathbf{X}) = \mathbf{F}_\text{I} = \mathbf{F}_\text{N}, \quad \text{deformation gradient that maps material points in reference}$$

$$\text{to points } (\mathbf{x} = \varphi(\mathbf{X}), \varphi: \text{motion}) \text{ in deformed configuration;}$$

$$J = \det \mathbf{F} > 0, \qquad \text{volume change;}$$

$$\bar{\mathbf{F}}_\text{N} = J^{-1/3}\mathbf{F}_\text{N}, \qquad \text{isochoric part of } \mathbf{F}_\text{N};$$

$$\bar{\mathbf{B}}_\text{N} = \bar{\mathbf{F}}_\text{N}\bar{\mathbf{F}}_\text{N}^\top, \qquad \text{isochoric left Cauchy-Green tensor;}$$

$$\mathbf{F}_\text{I} = \mathbf{F}_\text{I}^\text{e}\mathbf{F}_\text{I}^\text{p}, \qquad \text{decomposition of } \mathbf{F}_\text{I} \text{ into its elastic and plastic parts;}$$

$$\mathbf{F}_\text{I}^\text{e} = \mathbf{R}_\text{I}^\text{e}\mathbf{U}_\text{I}^\text{e}, \qquad \text{polar decomposition of } \mathbf{F}_\text{I}^\text{e} \text{ into elastic rotation and stretch tensors;}$$

$$\mathbf{T}_\text{N}, \qquad \text{Cauchy stress in the N mechanism;}$$

$$\mathbf{T}_\text{I}, \qquad \text{Cauchy stress in the I mechanism.} \tag{1}$$

The deformation rate is described by the velocity gradient $\mathbf{L} \overset{\text{def}}{=} \text{grad}\,\mathbf{v} = \mathbf{L}_\text{I}$ which is decomposed into elastic ($\mathbf{L}_\text{I}^\text{e}$) and plastic ($\mathbf{L}_\text{I}^\text{p}$) parts,

$$\begin{aligned}
\mathbf{L}_\text{I} &= \dot{\mathbf{F}}_\text{I}\mathbf{F}_\text{I}^{-1} \\
&= \dot{\mathbf{F}}_\text{I}^\text{e}\mathbf{F}_\text{I}^{\text{e}-1} + \mathbf{F}_\text{I}^\text{e}\dot{\mathbf{F}}_\text{I}^\text{p}\mathbf{F}_\text{I}^{\text{p}-1}\mathbf{F}_\text{I}^{\text{e}-1} \\
&= \mathbf{L}_\text{I}^\text{e} + \mathbf{F}_\text{I}^\text{e}\mathbf{L}_\text{I}^\text{p}\mathbf{F}_\text{I}^{\text{e}-1}.
\end{aligned} \tag{2}$$

Here, the plastic part of the velocity gradient is $\mathbf{L}_\text{I}^\text{p} = \mathbf{D}_\text{I}^\text{p} + \mathbf{W}_\text{I}^\text{p}$, where $\mathbf{D}_\text{I}^\text{p}$ is the rate of plastic stretching and $\mathbf{W}_\text{I}^\text{p}$ is the plastic spin. We make two important kinematical assumptions for the plastic flow; the flow is incompressible, i.e. $J^\text{p} \overset{\text{def}}{=} \det \mathbf{F}_\text{I}^\text{p} = 1$ and irrotational, i.e. $\mathbf{W}_\text{I}^\text{p} = \mathbf{0}$. Thus, the rate of change in the plastic deformation gradient is given by,

$$\dot{\mathbf{F}}_\text{I}^\text{p} = \mathbf{D}_\text{I}^\text{p}\mathbf{F}_\text{I}^\text{p}. \tag{3}$$

The Mandel stress in the time-dependent mechanism, I, is expressed by,

$$\mathbf{M}_I^e = 2\mu_I \left(\mathbf{E}_I^e\right)_0 + K \operatorname{tr}\left(\mathbf{E}_I^e\right)\mathbf{I} \quad \text{where} \quad \mathbf{E}_I^e = \ln\mathbf{U}_I^e \quad \text{and} \quad (\mathbf{E}_I^e)_0 = \mathbf{E}_I^e - \frac{1}{3}\operatorname{tr}(\mathbf{E}_I^e)\mathbf{I}. \tag{4}$$

The Cauchy stress in the time-dependent mechanism, I, is then related to the Mandel stress by,

$$\mathbf{T}_I = J^{-1}\mathbf{R}_I^e\mathbf{M}_I^e\mathbf{R}_I^\top, \tag{5}$$

with the shear modulus μ_I and the bulk modulus K in the hard material. The rate of plastic stretching $\mathbf{D}_I^p$ is assumed to be coaxial to the Mandel stress given in Eq. (4),

$$\mathbf{D}_I^p = \frac{\dot{\gamma}^p}{\sqrt{2}}\mathbf{N}_I^p \quad \text{where} \quad \mathbf{N}_I^p = \frac{(\mathbf{M}_I^e)_0}{\|(\mathbf{M}_I^e)_0\|} \quad \text{and} \quad \|(\mathbf{M}_I^e)_0\| = \sqrt{(\mathbf{M}_I^e)_0 : (\mathbf{M}_I^e)_0}. \tag{6}$$

Here, the magnitude of plastic flow, $\dot{\gamma}^p$, is prescribed by a thermally-activated viscoplasticity model,

$$\dot{\gamma}^p = \dot{\gamma}_0 \exp\left[-\frac{\Delta G}{k\theta}\left\{1 - \frac{\bar{\tau}_I}{s_0}\right\}\right] \quad \text{where} \quad \bar{\tau}_I = \frac{1}{\sqrt{2}}\|(\mathbf{M}_I^e)_0\| \tag{7}$$

with the reference plastic shear strain rate $\dot{\gamma}_0$, the activation energy ΔG, the shear resistance s_0, Boltzmann's constant k and the absolute temperature θ (in this work, an isothermal condition was assumed with room temperature, $\theta = 295$ K). Furthermore, $\bar{\tau}_I = \frac{1}{\sqrt{2}}\|(\mathbf{M}_I^e)_0\|$ is the magnitude of the deviatoric part of the Mandel stress, also known as, the Mises equivalent stress.

The time-independent mechanism is represented by an Arruda-Boyce model.[1] The Cauchy stress is expressed by,

$$\mathbf{T}_N = \frac{\mu_N}{3J}\left(\frac{\lambda_N}{\bar{\lambda}}\right)\mathscr{L}^{-1}\left(\frac{\bar{\lambda}}{\lambda_N}\right)(\bar{\mathbf{B}}_N)_0 \quad \text{where} \quad \bar{\lambda} = \sqrt{\frac{\operatorname{tr}\left(\bar{\mathbf{B}}_N\right)}{3}} \quad \text{and} \quad \mathscr{L}(x) = \coth(x) - x^{-1} \tag{8}$$

with the shear modulus μ_N and the limiting chain extensibility $\lambda_N = \sqrt{N_N}$ where N_N is the average number of effective chain segments.

The total stress of the hard material is given by,

$$\mathbf{T}_{\text{Hard}} = \mathbf{T}_I + \mathbf{T}_N. \tag{9}$$

Here, it should be noted that the time-independent mechanism, N, is taken to be deviatoric (Eq. (8)) so that the bulk response in the hard material is simply lumped into the time-dependent mechanism, I.

For the soft material, we have used a nearly incompressible Arruda-Boyce model. The deviatoric part of the isochoric left Cauchy-Green tensor is expressed by,

$$\bar{\mathbf{B}}_0 = \bar{\mathbf{B}} - \frac{1}{3}\,\mathrm{tr}(\bar{\mathbf{B}})\mathbf{I} \quad \text{where} \quad \bar{\mathbf{B}} = \bar{\mathbf{F}}\bar{\mathbf{F}}^\top \text{ and } \bar{\mathbf{F}} = J^{-1/3}\mathbf{F}. \tag{10}$$

The Cauchy stress can be then expressed by,

$$\mathbf{T}_{\mathrm{Soft}} = \frac{\mu_{\mathrm{S}}}{3J}\left(\frac{\lambda_{\mathrm{S}}}{\bar{\lambda}}\right)\mathscr{L}^{-1}\left(\frac{\bar{\lambda}}{\lambda_{\mathrm{S}}}\right)\bar{\mathbf{B}}_0 + K_{\mathrm{S}}\left(J-1\right)\mathbf{I} \quad \text{where} \quad \bar{\lambda} = \sqrt{\frac{\mathrm{tr}\left(\bar{\mathbf{B}}\right)}{3}}, \tag{11}$$

with the shear modulus μ_{S}, the limiting chain extensibility $\lambda_{\mathrm{S}} = \sqrt{N_{\mathrm{S}}}$ where N_{S} is the average number of effective chain segments and the bulk modulus K_{S} in the soft material.

Fig. S2 show the stress-strain curves numerically simulated using the constitutive models for both hard and soft materials. As shown, the constitutive models capture the overall "plastomeric" and "elastomeric" features in hard and soft materials upon loading and unloading observed in experiments reasonably well. The material parameters used in the constitutive models are given in Table S1. We then numerically implemented the finite deformation constitutive model for the hard material for use in the finite element solver for the micromechanical analysis throughout this paper; for the soft material, we simply used an approximate Arruda-Boyce representation provided in Abaqus/Standard. Detailed information on the time integration procedures for the time-dependent mechanism, I, in the hard material can be found in Weber and Anand (1990).[2]
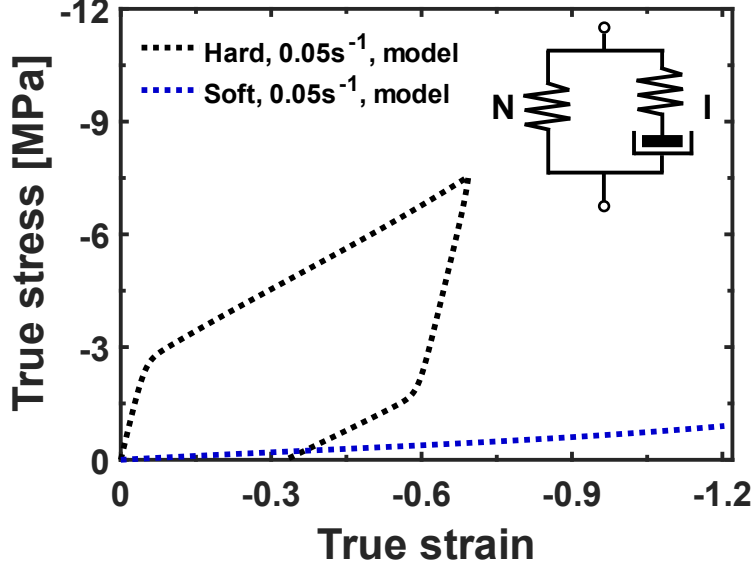
Fig. S2: Stress-strain behavior of the hard material (black dashed line) and the soft material (blue dashed line) at a strain rate of 0.05 s^{-1} in model.

Hard domain: time-dependent component			
$\mathbf{T}_{\mathrm{I}} = J^{-1}\mathbf{R}_{\mathrm{I}}^{\mathrm{e}}\mathbf{M}_{\mathrm{I}}^{\mathrm{e}}\mathbf{R}_{\mathrm{I}}^{\mathrm{e}\top}$ where $\mathbf{M}_{\mathrm{I}}^{\mathrm{e}} = 2\mu_{\mathrm{I}}\left(\mathbf{E}_{\mathrm{I}}^{\mathrm{e}}\right)_0 + \mathrm{K}\,\mathrm{tr}\left(\mathbf{E}_{\mathrm{I}}^{\mathrm{e}}\right)\mathbf{I}$	μ_{I}	[MPa]	15.8
	K	[GPa]	0.904
$\dot{\gamma}^{\mathrm{p}} = \dot{\gamma}_0 \exp\left[-\frac{\Delta G}{k\theta}\left\{1 - \frac{\bar{\tau}_{\mathrm{I}}}{s_0}\right\}\right]$	ΔG	$[10^{-20}\mathrm{J}]$	2.48
	$\dot{\gamma}_0$	$[s^{-1}]$	0.159
	s_0	[MPa]	1.44
Hard domain: time-independent component			
$\mathbf{T}_{\mathrm{N}} = \frac{\mu_{\mathrm{N}}}{3J}\left(\frac{\lambda_{\mathrm{N}}}{\bar{\lambda}}\right)\mathscr{L}^{-1}\left(\frac{\bar{\lambda}}{\lambda_{\mathrm{N}}}\right)\left(\bar{\mathbf{B}}_{\mathrm{N}}\right)_0$	μ_{N}	[MPa]	2.37
	N_{N}		6
Soft domain			
$\mathbf{T}_{\mathrm{Soft}} = \frac{\mu_{\mathrm{S}}}{3J}\left(\frac{\lambda_{\mathrm{S}}}{\bar{\lambda}}\right)\mathscr{L}^{-1}\left(\frac{\bar{\lambda}}{\lambda_{\mathrm{S}}}\right)\bar{\mathbf{B}}_0 + K_{\mathrm{S}}\left(J-1\right)\mathbf{I}$	μ_{S}	[MPa]	0.23
	N_{S}		10
	K_{S}	[MPa]	16.4

Table S1: Material parameters used in the constitutive models for hard and soft materials.

2 Constructing representative volume elements

The large strain behaviors of heterogeneous soft crystals were analyzed via micromechanical modeling. To this end, the corresponding representative volume elements (RVE) for SC, BCC and FCC in the major crystallographic orientations (<100>, <110> and <111>) were identified throughout this work. Here, we present a simple procedure to identify the suitable RVEs of SC, BCC and FCC. Consider, for example, a non-trivial case for generating an RVE for BCC-inter in the <111> direction. Fig. S3a depicts the cross-section on (111) plane of bulk BCC-inter. Each region (rectangle) on the cross-section is the representative "surface" element on the plane. Fig. S3b shows the side view of a rectangular parallelepiped along the depth direction <111> in the red region in Fig. S3a. Similarly, the blue region in Fig. S3b is the representative "surface" element of the lateral plane. Then, the corresponding RVE (blue region) for this particular BCC-inter in the <111> direction is identified, ensuring the periodicity in three dimensions. For other crystallographic orientations and crystal lattices, RVEs have been constructed, using a similar procedure.
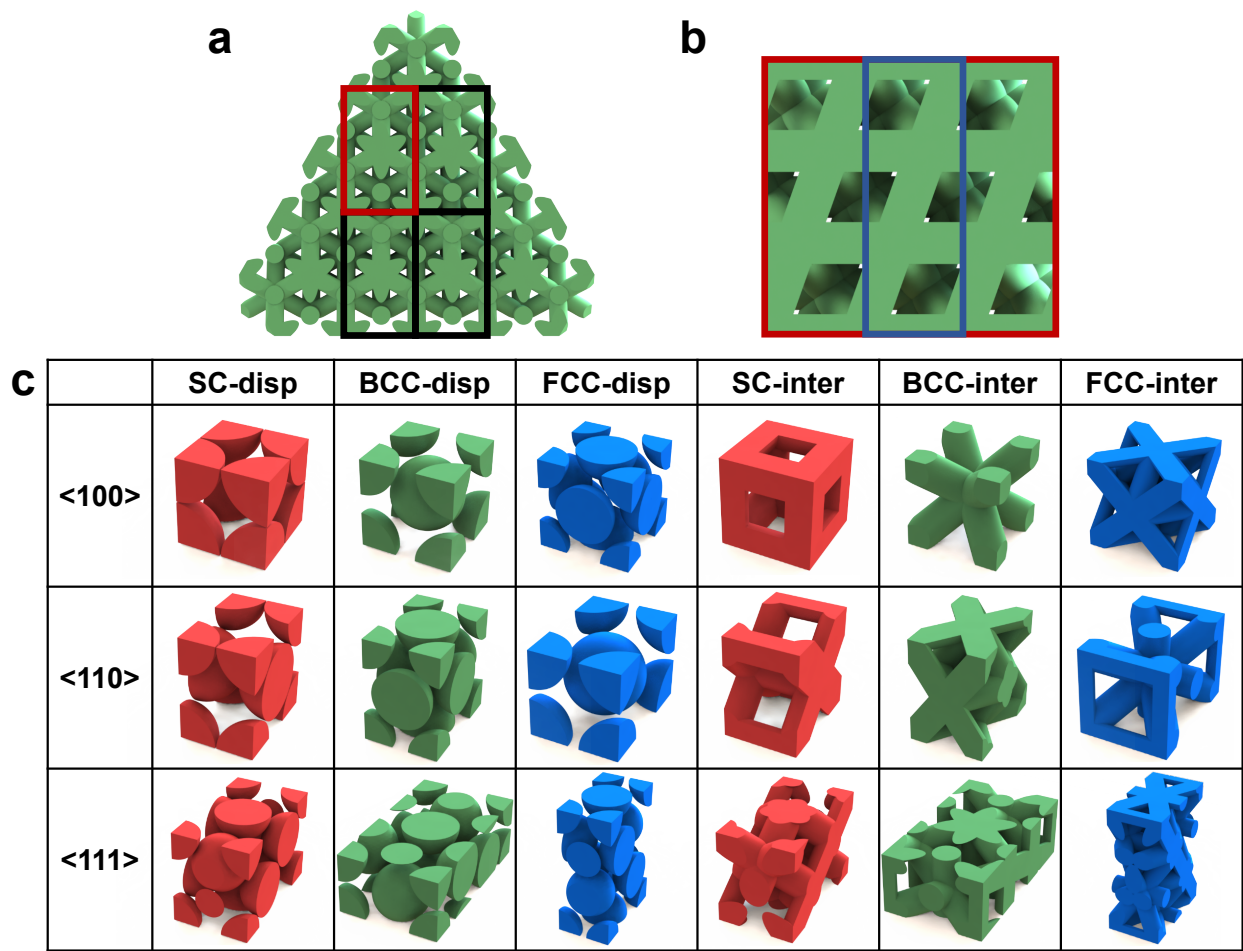
Fig. S3: Identification of representative volume elements in SC, BCC and FCC lattices. (a) Cross-section of a bulk BCC-inter on (111) plane and (b) rectangular parallelepiped along the depth direction, <111>. Identified RVEs (loading direction: normal to the top surface) in SC, BCC and FCC lattices: (c) dispersed-particle and interpenetrating morphologies. Here only hard domains are shown.

3 Constituent materials vs. heterogeneous soft crystals

Dissipated energy and elastic shape recovery in the SC and BCC materials with and without connectivity were found to be between those in the "pure" hard and soft constituent materials, as shown in Fig. S4. The results clearly support that the heterogenous materials presented in this work take advantages from both hard (energy dissipation) and soft (shape recovery) constituents.
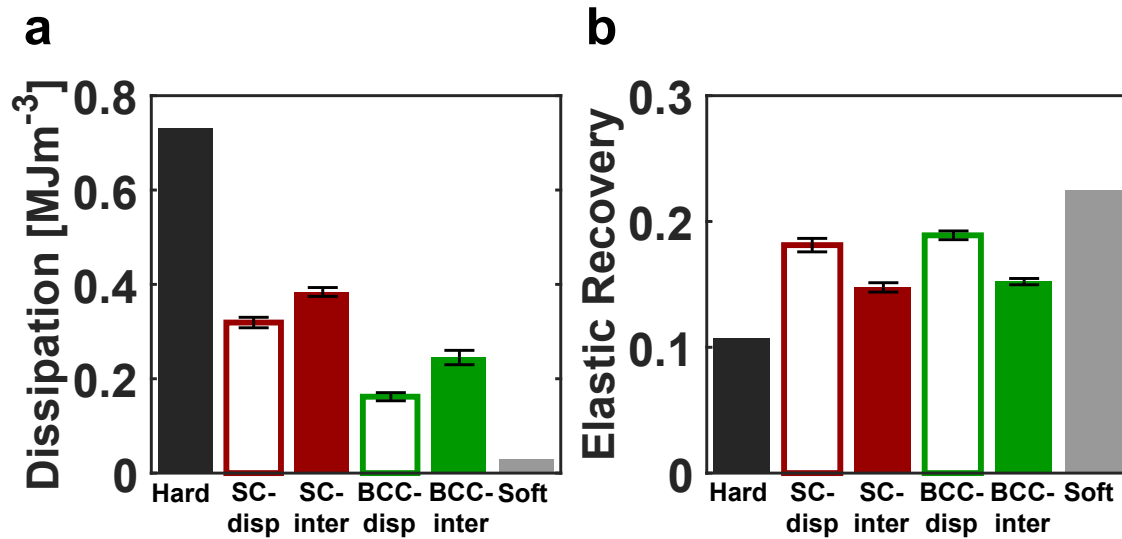

Fig. S4: Constituent materials vs. heterogeneous soft crystals. (a) Energy dissipation and (b) elastic recovery to an imposed strain of 0.3 at a strain rate of 0.05 s^{-1}. The error bars represent the standard deviations from experimental data of five samples.

4 Deformation fields in soft domains in SC and BCC materials with $V_\mathrm{h} = 50\%$

The effect of adding connectivity is further examined through the local axial stress contours in soft domains in the BCC materials (Fig. S5a and S5b) and SC materials (Fig. S5c and S5d) with a relatively high fraction of the hard components ($V_\mathrm{h} = 50\%$) loaded in the <100> direction (see Fig. 3 in the main body of the manuscript). As shown in Fig. S5a and S5c, in the dispersed-particle SC and BCC materials, the soft domains between the co-axial hard particles significantly deforms from the early stage of loading. Initially, the overall deformation is mainly carried by the soft domains, and the stress developed in the soft domain is transferred to the top and bottoms of the hard particles (see the very large compressive stress development throughout the soft ligaments between the co-axial hard particles in Fig. S5a2 and S5c2). This observation can be further supported by additional numerical simulations on BCC-disp and SC-disp with a "stiffer" soft domain (here, $\frac{E_\mathrm{hard}}{E_\mathrm{soft}}$ was taken to be ~ 7; it was ~ 70 throughout the main results presented in the manuscript), for which the material parameters of the hard component were fixed. As shown in Fig. S5e, highly hysteretic behavior with much more energy dissipation was available in both BCC-disp and SC-disp with the greater elastic modulus in the soft domain ($\frac{E_\mathrm{hard}}{E_\mathrm{soft}} \sim 7$). As the soft domain becomes stiffer, more of the imposed macroscopic deformation is accommodated by the hard particles in the composite materials, resulted in stronger inelastic flow throughout the hard particles and, consequently, more energy dissipation. However, the deformation is mainly carried by the hard ligament networks from the early stage of loading in the interpenetrating materials as shown in the axial stress contours displayed in Fig. S5b and S5d. The significant deformation throughout the hard ligament networks is responsible for the stiffening effect due to added connectivity from dispersed to interpenetrating morphologies presented in the macroscopic stress-strain responses presented in Fig. 3 and 4 in the main body of the manuscript.
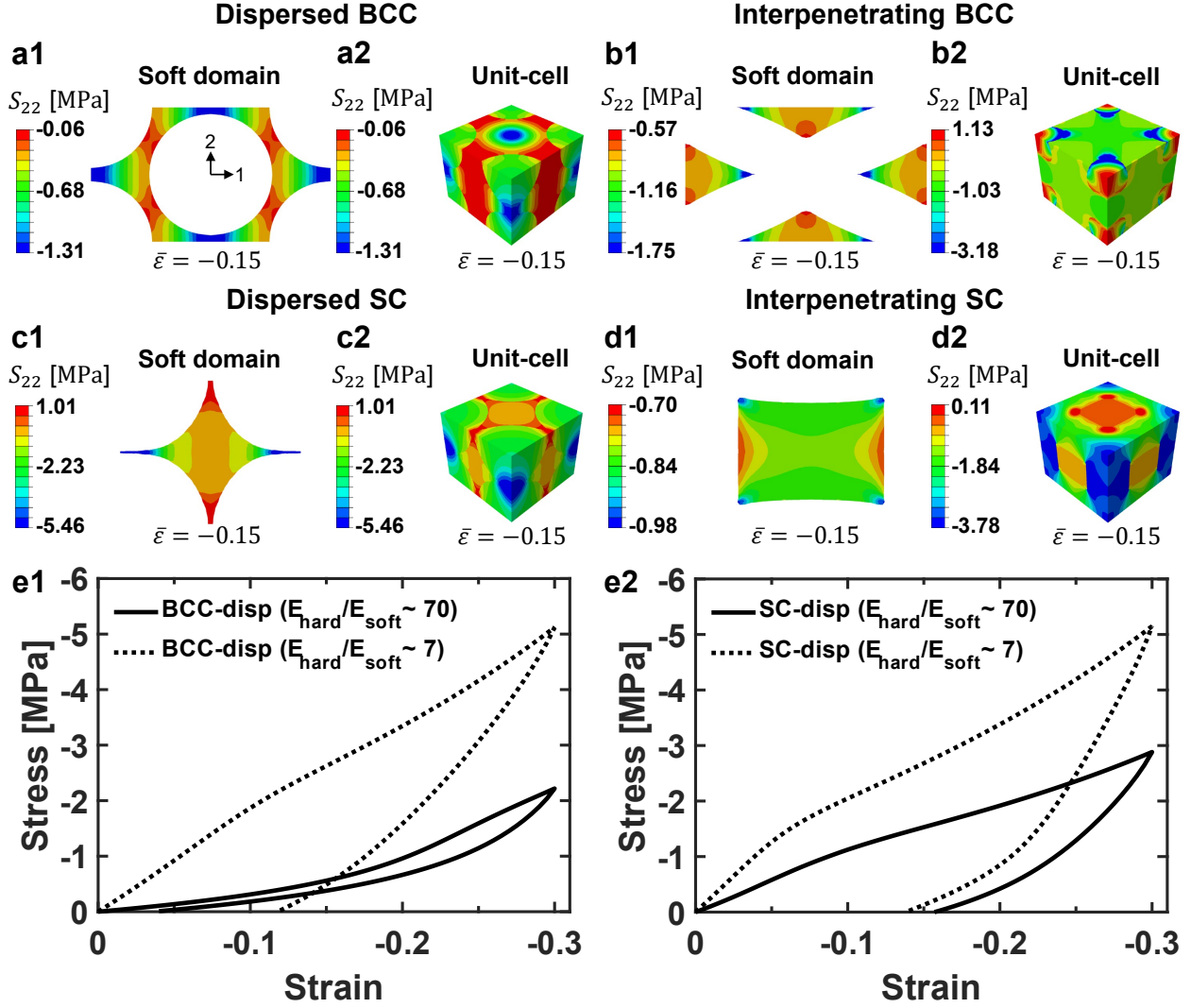
Fig. S5: Contours of axial stress at a compressive strain of 0.15 in soft domains in (a1) BCC-disp, (b1) BCC-inter, (c1) SC-disp and (d1) SC-inter loaded in the <100> direction. Here, the cutting plane to aid visualization for BCC (a1, b1) and SC (c1, d1) materials are taken to be (110) and (100) on the unit-cell, respectively. Isometric views of unit-cells of both hard and soft domains with axial stress contours for (a2) BCC-disp, (b2) BCC-inter, (c2) SC-disp and (d2) SC-inter loaded in <100> direction. Simulated stress-strain curves of (e1) BCC-disp and (e2) SC-disp loaded in <100> direction with $\frac{E_{\text{hard}}}{E_{\text{soft}}} \sim 70$ and 7.

11

5 FCC-disp vs. FCC-inter loaded in the <100> and <110> directions; $V_h = 50\%$

Fig. S6 presents the large strain behaviors of the dispersed-particle and interpenetrating FCC (FCC-disp and FCC-inter; $V_h = 50\%$) loaded in the <100> and <110> directions in both experiments and numerical simulations. Similar to the SC and BCC materials, the FCC-inter exhibits the greater macroscopic stress and energy dissipation than those in FCC-disp in both loading directions (Fig. S6a1 and S6b1). The effect of adding connectivity (from the dispersed-particle to interpenetrating morphology) on elastic modulus and energy dissipation was more significant when these materials were loaded in the bending-dominated direction, herein for FCC, <100> (Fig. S6a2, S6a3, S6b2 and S6b3).
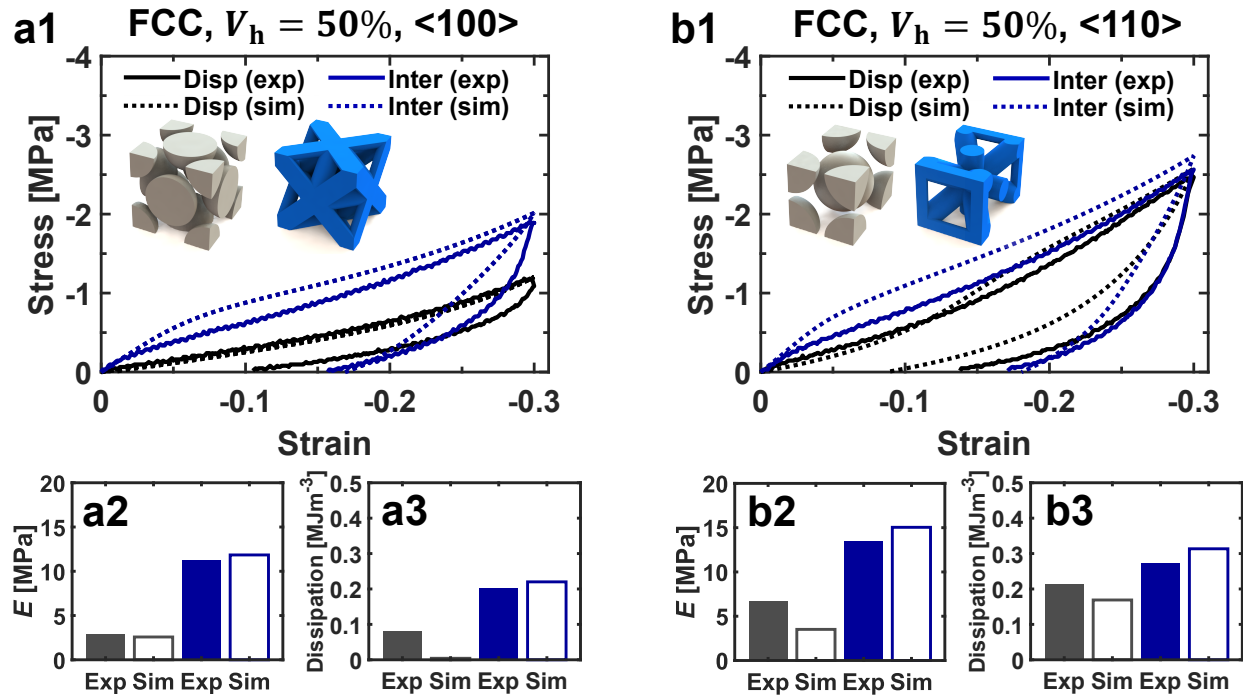

Fig. S6: Effects of connectivity change in FCC materials from dispersed-particle to interpenetrating morphologies on initial elastic modulus, flow stresses and energy dissipation. The volume fraction of hard component was $V_h = 50\%$. Stress-strain curves, elastic modulus and energy dissipation of FCC-disp (gray) and FCC-inter (blue) loaded in the (a) <100> and (b) <110> directions (solid lines: experiment, dashed lines: simulation; insets: hard domain in each unit-cell).

6   SC-disp vs. SC-inter and BCC-disp vs. BCC-inter in the <111> and <100> directions; $V_h = 25\%$

In the BCC (Fig. S7a1, S7a2 and S7a3) and SC (Fig. S7b1, S7b2 and S7b3) materials loaded in the bending-dominated directions (<100> and <111> for BCC and SC, respectively), the effect of adding connectivity on both elastic stiffness and energy dissipation decreased significantly. This result has been observed in the materials with a relatively low fraction of the hard components ($V_h = 25\%$), as evidenced in both experiments and numerical simulations.

Fig. S7: Effect of connectivity change in BCC and SC material from dispersed-particle to interpenetrating morphologies on initial elastic modulus, flow stresses and energy dissipation. The volume fraction of hard component was $V_h = 25\%$. Stress-strain curves, elastic modulus and energy dissipation of (a) BCC-disp (gray) and BCC-inter (green) loaded in the <100> direction and (b) SC-disp (gray) and SC-inter (red) loaded in the <111> direction (solid lines: experiment, dashed lines: simulation; insets: hard domain each unit cell).

7 Inelastic shape recovery mechanism in hard constituent materials

Fig. S8a schematically shows a shape recovery process in the hard material in cyclic deformation. Remarkable shape recovery can be achieved in a few minutes after the end of unloading, as schematically illustrated in Fig. S8b. The shape recovery mechanism can be explained by the breakdown of total stress (Fig. S8c) into individual stress components of a time-independent mechanism (Fig. S8d) and a time-dependent mechanism (Fig. S8e); though the total stress is zero at the end of unloading, the individual stress component of the time-dependent mechanism still has a "finite" magnitude with an opposite sign to that of the time-independent mechanism. Non-zero stress in the time-dependent mechanism hence drives inelastic flow which leads to additional shape recovery beyond elastic recovery during unloading. During "inelastic" recovery, the total stress is kept to zero due to mutual balancing between the time-dependent elastic-inelastic mechanism I and network elastic mechanism N, as shown in Fig. S8f.
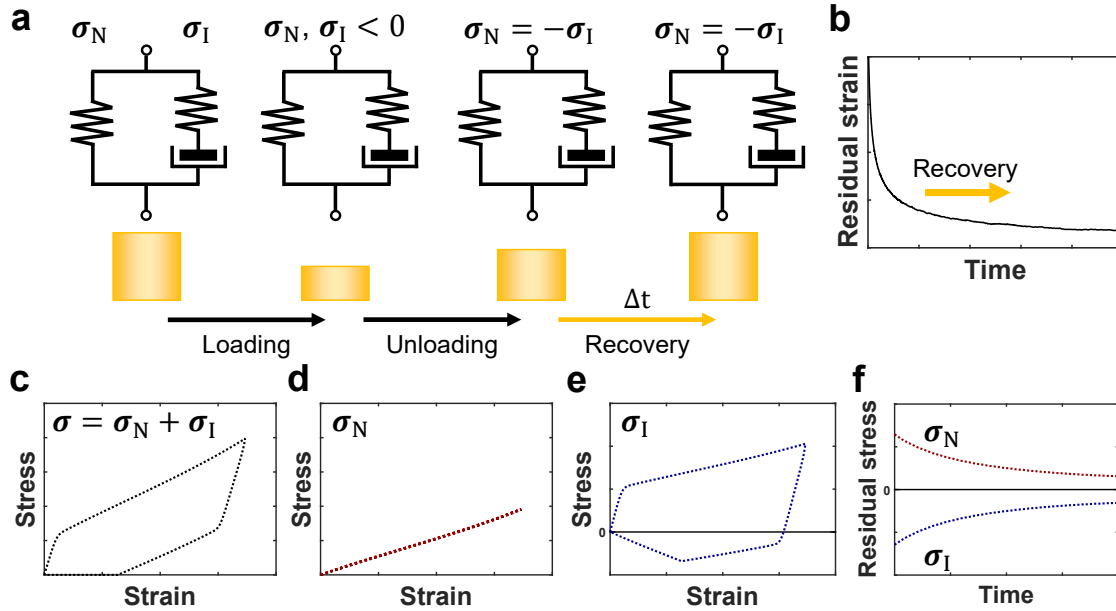

Fig. S8: Shape recovery mechanism in hard constituent materials: (a) schematics of shape recovery process under cyclic loading condition, (b) residual strain vs. time during inelastic recovery, (c) total stress vs. strain, (d) stress in time-independent mechanism N, (e) stress in time-dependent elastic-inelastic mechanism I and (f) individual stress components in I and N vs. time during inelastic recovery.
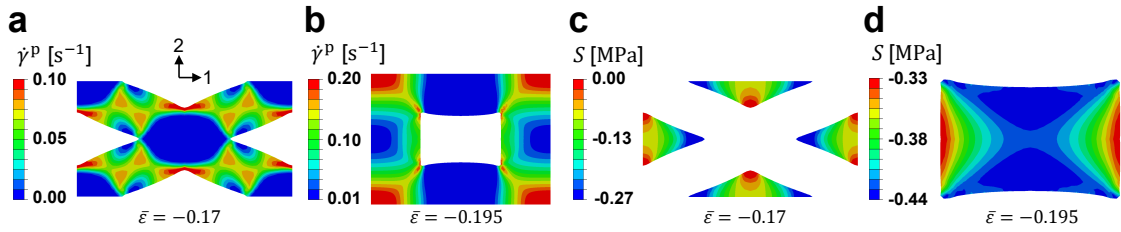
Fig. S9: Contours of inelastic strain rate in hard domains in (a) BCC-inter and (b) SC-inter, and contours of axial stress in soft domains in (c) BCC-inter and (d) SC-inter at the end of unloading (see Figure 5b1 and 5b2 in the main text). The volume fraction of hard components is $V_\mathrm{h} = 50\%$ and the strain rate is 0.05 s^{-1}. Here, the cutting planes for BCC (a, c) and SC (b, d) materials were taken to be (110) and (100), respectively.

8 Relative elastic modulus and dissipation in SC-inter and BCC-inter

Fig. S10 shows the elastic modulus and energy dissipation in each crystallographic orientation relative to those in the stretching-dominated direction (<100> and <111> in SC and BCC). The magnitude of the relative elastic modulus is comparable to that in the relative energy dissipation throughout all of the crystallographic orientations in both SC-inter and BCC-inter. These micromechanical modeling results also support the hypothesis that the elastic modulus during the early stage of loading can be used to estimate the energy dissipation that involves the complex unloading behavior in these elasto-plastomeric heterogeneous materials subjected to large strains.
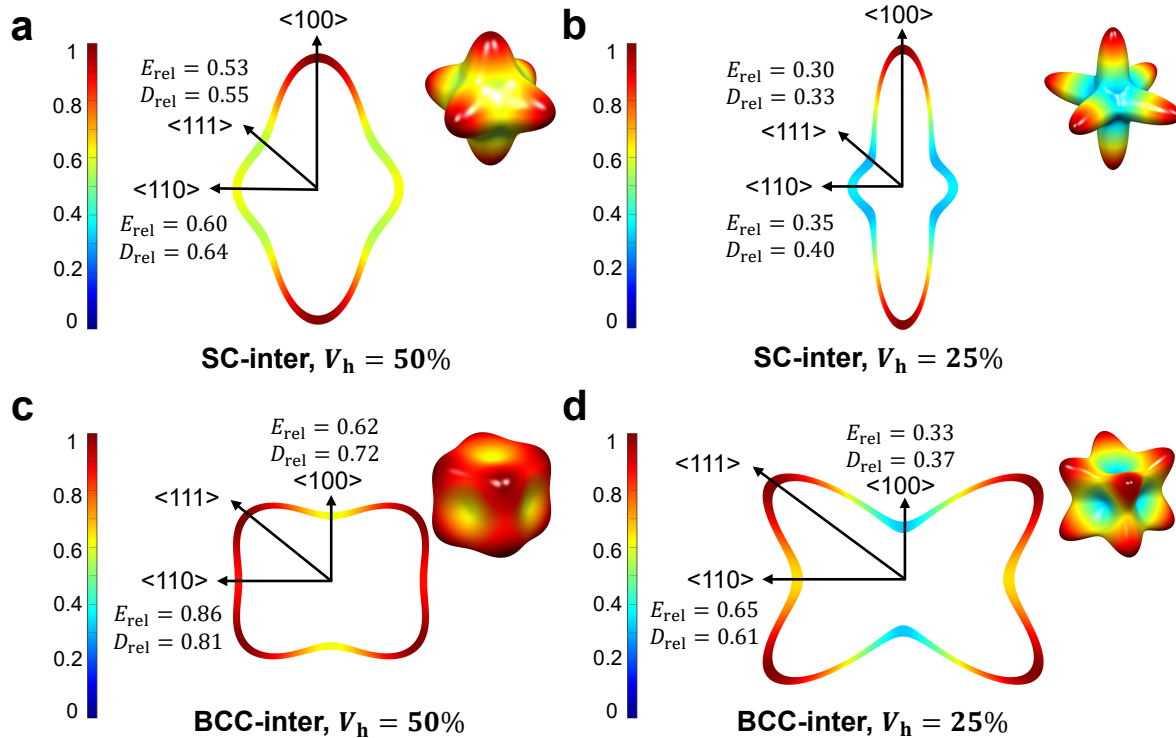

Fig. S10: Micromechanical modeling results of elastic and inelastic anisotropy maps in (a) SC-inter, $V_h = 50\%$, (b) SC-inter, $V_h = 25\%$, (c) BCC-inter, $V_h = 50\%$ and (d) BCC-inter, $V_h = 25\%$. The cutting plane to aid visualization is (110) on the center of the three-dimensional anisotropy maps. The directional elastic modulus relative to that in the stretching-dominated directions (maximum elastic modulus; <100> and <111> for SC and BCC, respectively) is represented by the magnitude of each vector on the surface. Additionally, relative elastic modulus and relative energy dissipation are denoted by and E_{rel} and D_{rel}.

9 Reusability under combined loading scenarios of impact and quasi-static cycles

The reusability, resilience and energy dissipation of the interpenetrating materials are further investigated upon combined loading scenarios of impact and quasi-static cycles in Fig. S11. As schematically presented in Fig. S11a, BCC-inter and SC-inter were first subjected to impact (with an indenter of 22 kg) in the drop-tower; then they were monitored during shape recovery for 10 minutes. Next, the prototypes were subjected to a loading and unloading cycle up to a maximum imposed strain of 0.4 at a low strain rate of 0.075 s^{-1}. Another idling time of 10 minutes for inelastic recovery was also taken prior to the next combined cycle of impact and low strain rate loading and unloading. Fig. S13 shows an experimental setup on the combined tests of impact and quasi-static cycles. As demonstrated in Fig. 8a2 and 8b2 in the main body of manuscript, both of the interpenetrating SC and BCC materials exhibited very consistent shape recovery and energy dissipation capabilities during multiple consecutive loading and unloading cycles along the <100> orientation (stretching-dominated for SC-inter and bending-dominated for BCC-inter) at low strain rates with no impact. However, as shown in Fig. S11b1 and Fig. S11b2 on SC-inter at the combined cycles of impact and quasi-static loading and unloading, the load transfer and energy dissipation capabilities significantly decreased as the combined cycle was repeated (from $N = 1$ to $N = 10$). Specifically, the SC-inter prototype exhibited $\sim 50\%$ degradation in the energy dissipation ability (Fig. S11b2) at $N = 10$, relative to $N = 1$. The repeated impact culminated in microstructural damage and breakdown throughout the rod-connected ligament network in the interpenetrating SC material especially along the "stiffest" stretching-dominated loading direction, <100>. By contrast, in the interpenetrating BCC material loaded in its bending-dominated direction, here <100>, it exhibited much more consistent capabilities in all of the load transfer, energy dissipation as well as shape recovery from $N = 1$ to $N = 10$ as presented in Fig. S11c1. More importantly, as shown in Fig. S11c2 on the dissipated energy density in BCC-inter as a function of the combined loading cycles, even at $N = 10$, it dissipated the applied strain energy by 71% of that in $N = 1$ (upon the first impact). This implies that the hard ligament network is responsible for the more robust performance in energy dissipation, resilience and load transfer via bending-dominated deformation modes especially upon the repeated impact loading scenarios. Through the bending-dominated deformation modes,

the interpenetrating, heterogeneous elasto-plastomeric materials can mitigate degradations in the resilience and dissipation capabilities in repeated, harsh mechanical conditions from quasi-static to impact loading regimes.
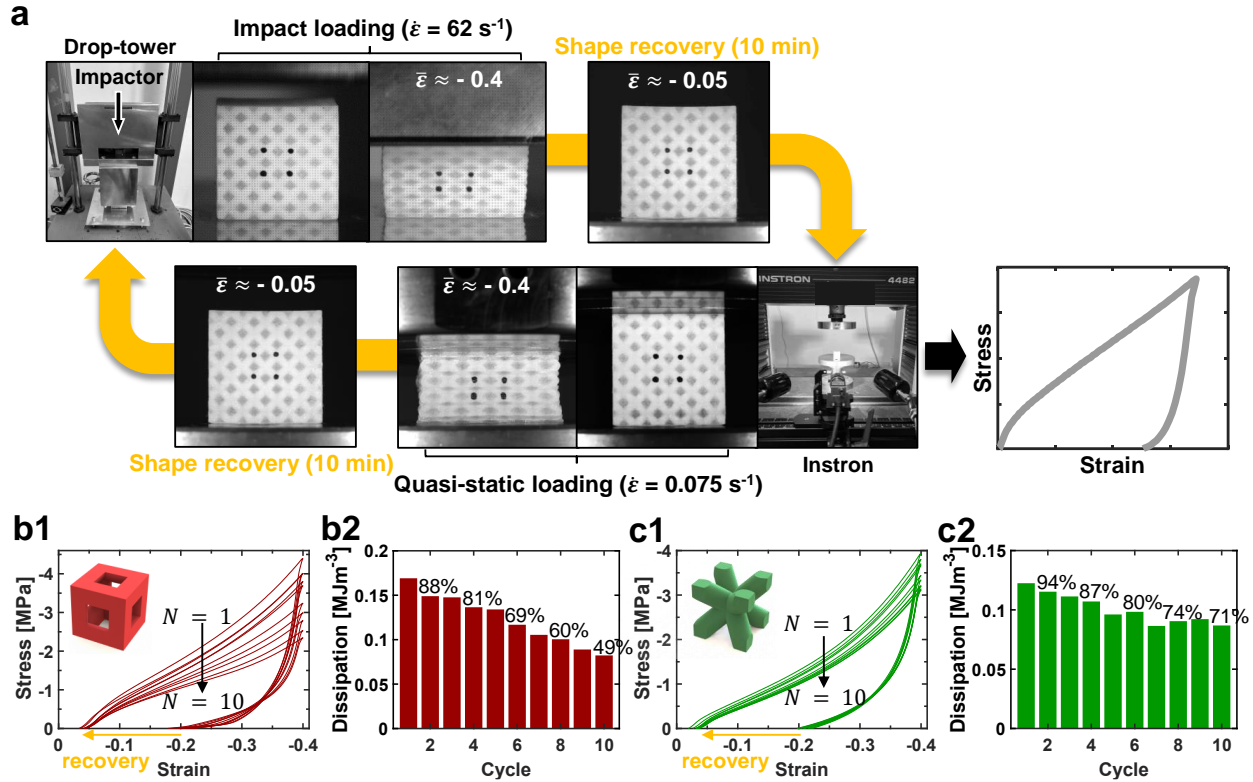

Fig. S11: Reusability of the heterogeneous elasto-plastomeric soft crystal in combined cycles (from $N = 1$ to $N = 10$) of impact and quasi-static loading and unloading up to a strain of 0.4. (a) Schematics of combined cycles of impact and quasi-static loading and unloading; the prototypes are first subjected to impact (imposed strain rate: $\sim 62\,\mathrm{s^{-1}}$; impactor: 22 kg); the prototypes are then subjected to a loading and unloading cycle up to a maximum imposed strain of 0.4 at a strain rate of $0.075\,\mathrm{s^{-1}}$. Between impact and quasi-static loading-unloading cycles, the idling time for inelastic recovery is taken to be 10 minutes. Stress-strain curves in (b1) SC-inter and (c1) BCC-inter from $N = 1$ to $N = 10$ in their stretching-dominated and bending-dominated directions. Energy dissipation in (b2) SC-inter and (c2) BCC-inter is also displayed from $N = 1$ to $N = 10$. Here, the numerical values indicate the dissipated work density in each cycle relative to that in $N = 1$ (upon the first impact).

10 Setup for drop-tower tests

Fig. S12 presents a schematic of a customized drop-tower used for impact tests of the prototypes presented in Fig. 6 in the main body of the manuscript and Fig. S11. The deformation process and transient shape recovery after impacts were monitored using a high-speed camera (Chronos 2.1-HD, Kron Technologies; SP 24-70mm F/2.8 lens, Tamron) capable of capturing 1,512 frames per second with a resolution of 1280 x 1024.
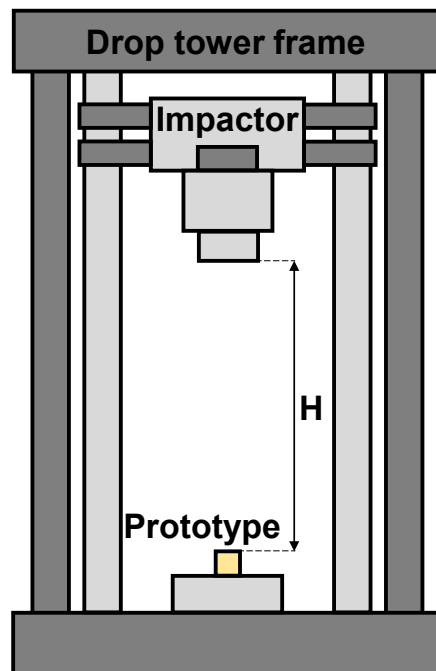

Fig. S12: Schematic of a rail-guided drop-tower. The initial height (denoted by H in the schematic) for dropping the impactor (22 kg) was taken to be 0.2 m and 0.7 m for impact tests.

N = 1 to N = 10

M = 22 kg
$\dot{\varepsilon} = 62$ s^{-1}

$\dot{\varepsilon} = 0.075$ s^{-1}

Impact **10 minutes recovery** **Quasi-static loading** **10 minutes recovery**

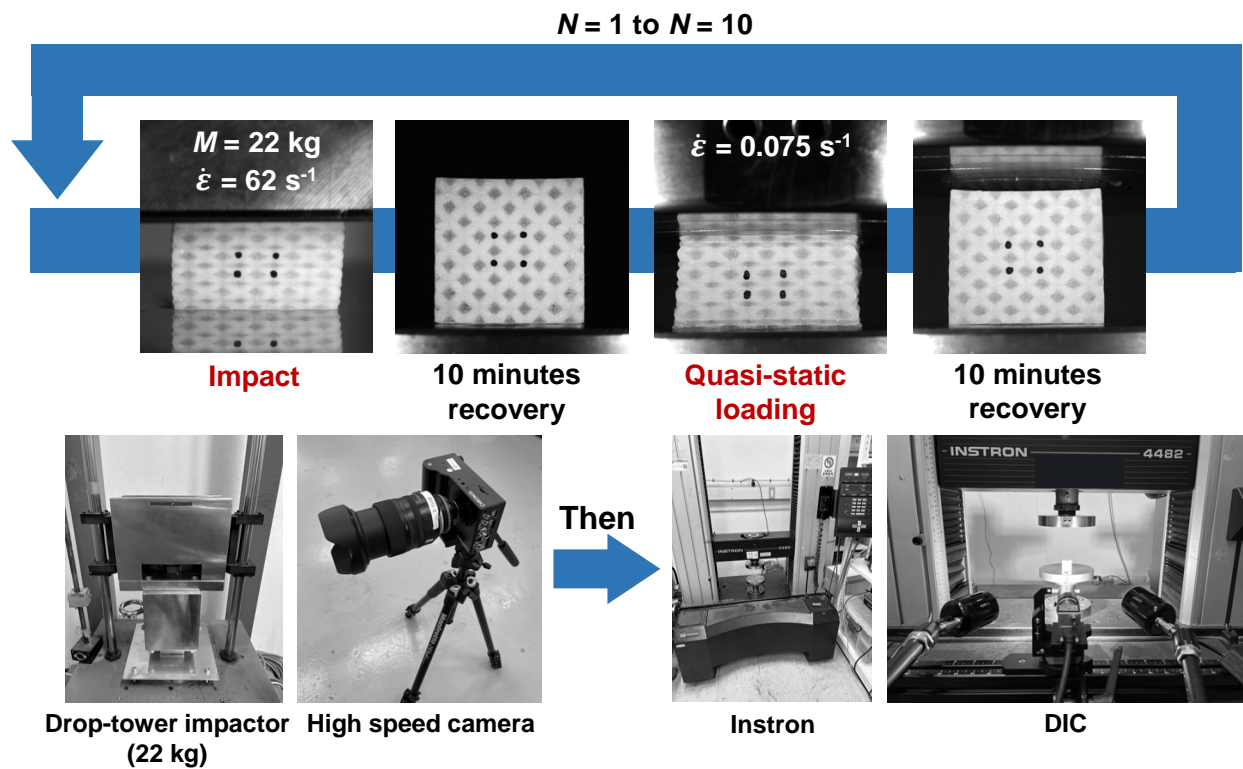**Drop-tower impactor (22 kg)** **High speed camera** **Then** **Instron** **DIC**

Fig. S13: Experimental setup for the combined tests of impact and quasi-static loading and unloading cycles presented in Fig. S11.

11 List of supplementary movies

- **Movie S1** shows the loading and unloading behavior of the SC-disp and SC-inter with a relatively high fraction of hard components ($V_h = 50\%$) loaded in the crystallographic orientation of <111> up to a maximum imposed strain of 0.3 ($\bar{\varepsilon} = -0.3$) at a strain rate of 0.05 s^{-1}. Macroscopic homogeneity of deformation throughout the periodic unit-cells in the prototypes was confirmed well. The speed of the video was taken to be increased by a factor of 2 (2x speed). Inset: the corresponding stress-strain curves in experiment.

- **Movie S2** shows the loading and unloading behavior of the BCC-disp and BCC-inter with a relatively high fraction of hard components ($V_h = 50\%$) loaded in the crystallographic orientation of <100> up to a maximum imposed strain of 0.3 ($\bar{\varepsilon} = -0.3$) at a strain rate of 0.05 s^{-1}. Macroscopic homogeneity of deformation throughout the periodic unit-cells in the prototypes was confirmed well. The speed of the video was taken to be increased by a factor of 2 (2x speed). Inset: the corresponding stress-strain curves in experiment.

- **Movie S3** shows the loading and unloading behavior, and shape recovery of the BCC-inter ($V_h = 50\%$) loaded in the <100> direction up to a maximum imposed strain of 0.3 ($\bar{\varepsilon} = -0.3$) at a strain rate of 0.05 s^{-1}. The red point moving on the stress-strain curve corresponds to the deformation state of the BCC-inter. The speed of the video was taken to be increased by a factor of 4 (4x speed). Thus, the actual time of the corresponding loading, unloading and recovery process is 90 seconds. The BCC-inter recovered its original shape up to a residual strain of 0.01 in 90 seconds.

- **Movie S4** shows the loading and unloading behavior, and shape recovery of the SC-inter ($V_h = 50\%$) loaded in the <100> direction up to a maximum imposed strain of 0.3 ($\bar{\varepsilon} = -0.3$) at a strain rate of 0.05 s^{-1}. The red point moving on the stress-strain curve corresponds to the deformation state of the SC-inter. The speed of the video was taken to be increased by a factor of 4 (4x speed). Thus, the actual time of the corresponding loading, unloading and recovery process is 90 seconds. The SC-inter recovered its original shape up to a residual strain of 0.02 in 90 seconds.

- **Movie S5** shows the deformation of the BCC-disp and BCC-inter ($V_h = 50\%$) loaded in the <111> direction up to a maximum imposed strain of 0.4 ($\bar{\varepsilon} = -0.4$) at a strain rate of 0.05 s^{-1} in the first ($N = 1$) and the last ($N = 8$) cycles. The speed of the video was taken to be increased by a factor of 2 (2x speed). The BCC-inter exhibited consistent stress-strain responses (the green curves) without buckling while the BCC-disp exhibited buckling during the multiple cycles of $N = 1$ to $N = 8$. The critical strain for buckling in the BCC-disp decreased in the subsequent cycles of $N = 2$ to $N = 8$ as shown in the insets on the stress-strain curves and the critical strains from $N = 1$ to $N = 8$.

- **Movie S6** shows the loading and unloading behavior, and shape recovery (10 minutes) of the BCC-inter loaded in the <100> direction up to a maximum imposed strain of 0.4 ($\bar{\varepsilon} = -0.4$) at a strain rate of 0.05 s^{-1} in the cycles of $N = 20, 25, 30, 35$ and 40. The consistent stress-strain responses were observed together with the consistent energy dissipation during the multiple loading, unloading and recovery cycles ($N = 1$ to $N = 40$).

- **Movie S7** shows loading and unloading behavior, and shape recovery of the SC-inter loaded in the <111> direction up to increasing, maximum imposed strains of 0.4 ($N = 5$, left), 0.5 ($N = 15$, center) and 0.6 ($N = 25$, right) at a strain rate of 0.05 s^{-1}. The SC-inter shows outstanding shape recovery during the multiple cycles of $N = 1$ to $N = 30$. However, the stress response and energy dissipation gradually decrease from the first cycle ($N = 1$). The speed of the video was taken to be increased by a factor of 4 (4x speed). Thus, the actual time of the video is 90 seconds.

- **Movie S8** shows loading and unloading behavior, and shape recovery of the FCC-inter loaded in the <100> direction up to increasing, maximum imposed strains of 0.4, 0.5 ($N = 15$, left), 0.6 ($N = 25$, center) and 0.7 ($N = 31$, right) at a strain rate of 0.05 s^{-1}. Consistent performance in load transfer, energy dissipation and shape recovery (stress-strain curves on the top left and energy dissipation on the top right) was observed during the multiple cycles of $N = 1$ to $N = 20$ ($\bar{\varepsilon} = -0.4 \sim -0.5$). Then, from the cycle of $N = 21$ (maximum imposed strain, $\bar{\varepsilon} = -0.6$), the stress response and energy dissipation gradually decrease. However, the FCC-inter still exhibits very nice shape recovery ability even at a maximum imposed strain of 0.7 ($N = 31$). The speed of the videos was taken to be increased by a factor of 4 (4x speed). Thus, the actual time of the video is 90

seconds. FCC-inter shows high reusability with remarkable shape recovery and consistent energy dissipation and load transfer capabilities during multiple loading, unloading and reloading cycles up to extreme imposed strains.

References

[1] Ellen M. Arruda and Mary C. Boyce. "A three-dimensional constitutive model for the large stretch behavior of rubber elastic materials". *Journal of the Mechanics and Physics of Solids* 41.2 (1993), pp. 389–412.

[2] Gustavo Weber and Lallit Anand. "Finite deformation constitutive equations and a time integration procedure for isotropic, hyperelastic-viscoplastic solids". *Computer Methods in Applied Mechanics and Engineering* 79.2 (1990), pp. 173–202.